Journal of the European Ceramic Society 38 (2018) 3578–3584

Contents lists available at ScienceDirect

Journal of the European Ceramic Society

journal homepage: www.elsevier.com/locate/jeurceramsoc

Original Article

High-entropy fluorite oxides

Joshua Gild[a], Mojtaba Samiee[b], Jeffrey L. Braun[c], Tyler Harrington[a], Heidy Vega[b], Patrick E. Hopkins[c], Kenneth Vecchio[a,b], Jian Luo[a,b,*]

[a] Program of Materials Science and Engineering, University of California, San Diego, La Jolla, CA 92093-0418, USA
[b] Department of NanoEngineering, University of California, San Diego, La Jolla, CA 92093-0448, USA
[c] Department of Mechanical and Aerospace Engineering, University of Virginia, Charlottesville, Virginia 22904, USA

ARTICLE INFO

Keywords:
High-entropy ceramic
Fluorite oxide
Thermal conductivity
Hardness
Sintering

ABSTRACT

Eleven fluorite oxides with five principal cations (in addition to a four-principal-cation ($Hf_{0.25}Zr_{0.25}Ce_{0.25}Y_{0.25}$)$O_{2-\delta}$ as a start point and baseline) were fabricated via high-energy ball milling, spark plasma sintering, and annealing in air. Eight of the compositions, namely ($Hf_{0.25}Zr_{0.25}Ce_{0.25}Y_{0.25}$)$O_{2-\delta}$, ($Hf_{0.25}Zr_{0.25}Ce_{0.25}$)($Y_{0.125}Yb_{0.125}$)$O_{2-\delta}$, ($Hf_{0.2}Zr_{0.2}Ce_{0.2}$)($Y_{0.2}Yb_{0.2}$)$O_{2-\delta}$, ($Hf_{0.25}Zr_{0.25}Ce_{0.25}$)($Y_{0.125}Ca_{0.125}$)$O_{2-\delta}$, ($Hf_{0.25}Zr_{0.25}Ce_{0.25}$)($Y_{0.125}Gd_{0.125}$)$O_{2-\delta}$, ($Hf_{0.2}Zr_{0.2}Ce_{0.2}$)($Y_{0.2}Gd_{0.2}$)$O_{2-\delta}$, ($Hf_{0.25}Zr_{0.25}Ce_{0.25}$)($Yb_{0.125}Gd_{0.125}$)$O_{2-\delta}$, and ($Hf_{0.2}Zr_{0.2}Ce_{0.2}$)($Yb_{0.2}Gd_{0.2}$)$O_{2-\delta}$, possess single-phase solid solutions of the fluorite crystal structure with high configurational entropies (on the cation sublattices), akin to those high-entropy alloys and ceramics reported in prior studies. Most high-entropy fluorite oxides (HEFOs), except for the two containing both Yb and Gd, can be sintered to high relative densities. These single-phase HEFOs exhibit lower electrical conductivities and comparable hardness (even with higher contents of softer components such as Y_2O_3 and Yb_2O_3), in comparison with 8 mol. % Y_2O_3-stabilized ZrO_2 (8YSZ). Notably, these single-phase HEFOs possess lower thermal conductivities than that of 8YSZ, presumably due to high phonon scattering by multiple cations and strained lattices.

1. Introduction

High-entropy alloys (HEAs), also known as complex concentrated alloys (CCAs) or multi-principal element alloys, typically consist of five or more principal elements in amounts ranging from 5 to 35 at. % [1,2]. The configurational entropy can reach a significant amount once five or more principal components are present in the system; it reaches a maximum value of $\Delta S_{mix} = R\ln N$ per mole for a N-component system, where R is the gas constant, for an equimolar composition. HEAs/CCAs, with intrinsically high lattice strain, are generally observed to possess lower thermal conductivity and higher hardness than their individual constituents [1,3]. HEAs/CCAs also exhibit a variety of other superior or promising properties [1,3].

Since the initial publications of HEAs/CCAs in 2004 by Yeh et al. [4] and Cantor et al. [5], studies of high-entropy metallic alloys have attracted great attention in the metallurgy community. In 2015, an entropy-stabilized oxide of the rocksalt crystal structure, ($Mg_{0.2}Zn_{0.2}Cu_{0.2}Co_{0.2}Ni_{0.2}$)O, was fabricated by Rost et al. [6], extending HEAs from metals to ceramics with ionic bonds. Further studies of this entropy-stabilized rocksalt oxide showed that doping aliovalent cations can lead to excellent lithium conductivity and enhanced dielectric constants [7,8]. It should be noted that prior studies have also fabricated high-entropy nitride and carbide films via reactive sputtering techniques [9,10]. More recently, high-entropy ultra-high temperature ceramics (HE-UHTCs), e.g., ($Hf_{0.2}Zr_{0.2}Ta_{0.2}Nb_{0.2}Ti_{0.2}$)$B_2$ and five other single-phase five-component metal diborides, and high-entropy functional ceramics, e.g., $Sr(Zr_{0.2}Sn_{0.2}Ti_{0.2}Hf_{0.2}Mn_{0.2})O_3$ and five other single-phase high-entropy perovskite oxides (HEPOs), have also been successfully synthesized [11,12]. Recent research efforts have been reported towards making multicomponent rare earth oxides [13], (Ti, Ta, Nb)C_xN_{1-x} cermets [14], and high-entropy thermoelectric materials [15].

Fluorite oxides are utilized for a variety of applications including solid ionic conductors, high temperature coatings, and catalysts [16–20]. The most widely-used fluorite oxides are based on zirconia (ZrO_2), hafnia (HfO_2), or ceria (CeO_2), and they are often doped with yttria (Y_2O_3) and/or various other oxide dopants (including rare earth oxides as well as MgO, CaO, and other oxides). This class of oxide materials often possess high oxygen conductivities, low thermal conductivities, high hardness, and high melting temperatures. In particular, rare earth doped zirconia and ceria are of great technological interest because of their high ionic or mixed conductivities as well as low thermal conductivities [16,17,19–21].

Specifically, high-entropy materials are of interest for their low

* Corresponding author at: Department of NanoEngineering, University of California, San Diego, La Jolla, CA 92093-0418, USA.
E-mail address: jluo@alum.mit.edu (J. Luo).

https://doi.org/10.1016/j.jeurceramsoc.2018.04.010
Received 6 February 2018; Accepted 7 April 2018
Available online 09 April 2018

thermal conductivity due to the possible scattering of phonons by multiple components and strained lattices. In this work, we examine the synthesis, phase stability (including the formation of high-entropy solid solutions), and selected properties of high-entropy fluorite oxides (HEFOs) consisting of solid solutions with equal molar fractions of HfO_2, ZrO_2, and CeO_2 as the base materials, as well as the additions of the oxides of Y, Yb, Ca, Ti, La, Mg, and Gd as fluorite phase stabilizers. We successfully synthesized eight single-phase, high-entropy, fluorite oxide solid solutions, namely, $(Hf_{0.25}Zr_{0.25}Ce_{0.25}Y_{0.25})O_{2-\delta}$, $(Hf_{0.25}Zr_{0.25}Ce_{0.25})(Y_{0.125}Yb_{0.125})O_{2-\delta}$, $(Hf_{0.2}Zr_{0.2}Ce_{0.2})(Y_{0.2}Yb_{0.2})O_{2-\delta}$, $(Hf_{0.25}Zr_{0.25}Ce_{0.25})(Y_{0.125}Ca_{0.125})O_{2-\delta}$, $(Hf_{0.25}Zr_{0.25}Ce_{0.25})(Y_{0.125}Gd_{0.125})O_{2-\delta}$, $(Hf_{0.2}Zr_{0.2}Ce_{0.2})(Y_{0.2}Gd_{0.2})O_{2-\delta}$, $(Hf_{0.25}Zr_{0.25}Ce_{0.25})(Yb_{0.125}Gd_{0.125})O_{2-\delta}$, and $(Hf_{0.2}Zr_{0.2}Ce_{0.2})(Yb_{0.2}Gd_{0.2})O_{2-\delta}$. The thermal and electrical conductivities, as well as hardness, of these materials are measured and compared with 8 mol. Y_2O_3-stabilized ZrO_2 (8YSZ) as a reference fluorite oxide. Notably, these single-phase HEFOs possess lower thermal conductivities than that of 8YSZ, due to high phonon scattering by the different masses and interatomic forces produced from the multiple cations.

2. Materials and methods

2.1. Synthesis and fabrication

To synthesize high-entropy fluorite oxides, powders of HfO_2, ZrO_2, CeO_2, TiO_2, Y_2O_3, Yb_2O_3, La_2O_3, Gd_2O_3, CaO, and MgO (≥99% purity; purchased from Alfa Aesar, MA, USA) were used as the starting materials. Appropriate amounts of five powders were weighted (calculated on a metals basis) and mixed to fabricate each composition of the targeted stoichiometry, listed Table 1.

We have examined 12 compositions. Each composition consists of an equal molar fraction of HfO_2, ZrO_2, and CeO_2 (either 25% or 20% on a metal basis) as the base material and includes one stabilizer (for Specimen HEFO1 with 25% Y_2O_3 as the only four-cation system) or two stabilizers of equal cationic fraction of 12.5% or 20%. In general, the five-cation compositions examined have the stoichiometry $(Hf_{0.25}Zr_{0.25}Ce_{0.25})(\alpha_{0.125}\beta_{0.125})O_{2-\delta}$ (Variant A) or $(Hf_{0.2}Zr_{0.2}Ce_{0.2})(\alpha_{0.2}\beta_{0.2})O_{2-\delta}$ (Variant B), where α and β represent two stabilizers. In general, we would not examine Variant B if Variant A did not form a single-phase HEFO. In addition to the four-cation composition HEFO1: $(Hf_{0.25}Zr_{0.25}Ce_{0.25}Y_{0.25})O_{2-\delta}$, 11 five-cation compositions (HEFO2A, HEFO3A, HEFO4A, HEFO4B, HEFO5A, HEFO5B, HEFO6A, HEFO7A, HEFO7B, HEFO8A, and HEFO8B) were examined in this study, where "A" or "B" refers to the Variant defined above. In addition, we also fabricated 8YSZ, Y_2O_3, and Yb_2O_3 as the reference materials. All compositions fabricated are listed in Table 1.

The raw powders were mixed via high-energy ball milling (HEBM) utilizing a SPEX 8000D mill (SpexCertPrep, NJ, USA) for 24 h in a silicon nitride jar with silicon nitride media. High-purity isopropyl alcohol was used to create a slurry for grinding to prevent caking of the powders in the milling containers. The HEBM was done in 30-minute intervals, interrupted by 10-minute cooling pauses to avoid overheating. The powders were then densified into 20-mm diameter disks via spark plasma sintering (SPS, Thermal Technologies, CA, USA) at 1800 °C for 5 min under a uniaxial pressure of 50 MPa with a heating ramping rate of 100 °C/min. The chamber was initially pumped down to vacuum of at least 10^{-2} Torr prior to the SPS experiments and flowed/flushed with argon gas at 700 °C to allow for off-gassing. The graphite die was lined with 125 μm thick graphite paper to prevent reaction of the specimen with the die. After SPS, the specimens were annealed in open air at 1500 °C for 12 h for decarburization. Most samples were subsequently annealed for 24 h at 1500 °C for homogenization and air-quenched or furnace cooled to room temperature for characterization and measurements. The samples fabricated for measuring thermal and electrical conductivity as well as hardness testing were furnace cooled (with the power shut down; instead of quenching to prevent microcracking), where the initial cooling rate was approximately 50 °C/min at 1500 °C.

2.2. Characterization

All specimens were characterized by X-ray diffraction (XRD) utilizing a Rigaku diffractometer with Cu Kα radiation.

Scanning electron microscopy (SEM) images and the corresponding energy dispersive X-ray (EDX) spectroscopy composition maps were collected from specimens of all compositions. The specimens were coated with carbon prior to analysis to prevent charging. The measurements were performed at an e-beam voltage of 20 kV to examine the higher energy peaks of Hf, Ce, and Gd for minimal convolution of the peaks. Due to the overlap between the Hf M_α and Si K_α peaks, the amount of Si contamination in the sample is unknown.

Densities were calculated from the measured mass and geometric

Table 1
All High Entropy Fluorite Oxides (HEFOs) fabricated, along with lattice parameters, densities, thermal conductivities, and Vicker's hardness values.

	Composition	Single Phase?	Lattice Parameter (Å)	Theoretical Density (g/cm^3)	Relative Density (Annealed)	Thermal Conductivity (W/m K)	Hardness (GPa)
HEFO1	$(Hf_{0.25}Zr_{0.25}Ce_{0.25})(Y_{0.25})O_{2-\delta}$	Y	5.24	7.22	98.5	1.74 ± 0.15	13.6 ± 0.5
HEFO2A	$(Hf_{0.25}Zr_{0.25}Ce_{0.25})(Y_{0.125}Ti_{0.125})O_{2-\delta}$	N	–	–	–	–	–
HEFO3A	$(Hf_{0.25}Zr_{0.25}Ce_{0.25})(Y_{0.125}Mg_{0.125})O_{2-\delta}$	N	–	–	–	–	–
HEFO4A	$(Hf_{0.25}Zr_{0.25}Ce_{0.25})(Y_{0.125}Yb_{0.125})O_{2-\delta}$	Y	5.23	7.68	100	1.55 ± 0.20	12.7 ± 0.7
HEFO4B	$(Hf_{0.2}Zr_{0.2}Ce_{0.2})(Y_{0.2}Yb_{0.2})O_{2-\delta}$	Y	5.24	7.88	93.7	1.29 ± 0.11	13.3 ± 0.6
HEFO5A	$(Hf_{0.25}Zr_{0.25}Ce_{0.25})(Y_{0.125}Ca_{0.125})O_{2-\delta}$	Y	5.25	7.48	98.5	1.1 ± 0.2	13.3 ± 0.6
HEFO5B	$(Hf_{0.2}Zr_{0.2}Ce_{0.2})(Y_{0.2}Ca_{0.2})O_{2-\delta}$	N	–	–	–	–	–
HEFO6A	$(Hf_{0.25}Zr_{0.25}Ce_{0.25})(Y_{0.125}La_{0.125})O_{2-\delta}$	N	–	–	–	–	–
HEFO7A	$(Hf_{0.25}Zr_{0.25}Ce_{0.25})(Y_{0.125}Gd_{0.125})O_{2-\delta}$	Y	5.25	9.22	96.4	1.17 ± 0.13	13.2 ± 0.5
HEFO7B	$(Hf_{0.2}Zr_{0.2}Ce_{0.2})(Y_{0.2}Gd_{0.2})O_{2-\delta}$	Y	5.28	9.87	95.8	1.61 ± 0.13	13.1 ± 0.5
HEFO8A	$(Hf_{0.25}Zr_{0.25}Ce_{0.25})(Yb_{0.125}Gd_{0.125})O_{2-\delta}$	Y	5.25	10.19	77.8	1.81 ± 0.14	12.6 ± 0.5
HEFO8B	$(Hf_{0.2}Zr_{0.2}Ce_{0.2})(Yb_{0.2}Gd_{0.2})O_{2-\delta}$	Y	5.27	11.52	68.4	1.62 ± 0.13	12.3 ± 0.7
8YSZ		Y		6.10	98.8	2.02 ± 0.17	13.2 ± 0.4
Y_2O_3		Y		5.01	99.8	–	6.9 ± 0.3
Yb_2O_3		Y		9.17	94.3	–	5.7 ± 0.3

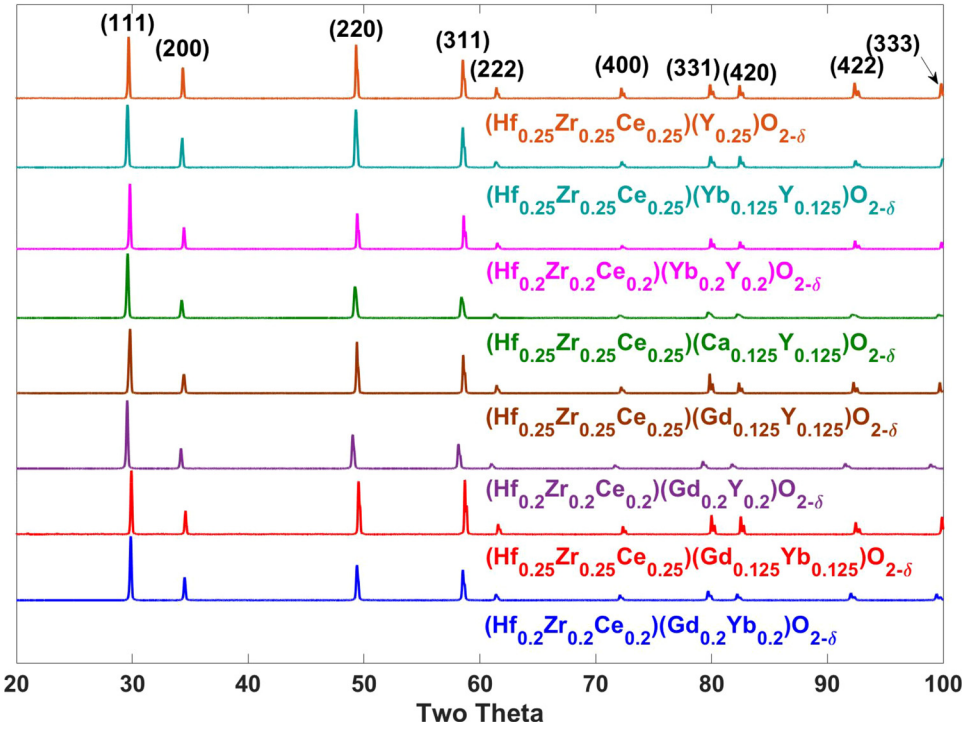

Fig. 1. XRD patterns of HEFO1: $(Hf_{0.25}Zr_{0.25}Ce_{0.25}Y_{0.25})O_{2-\delta}$, HEFO4A: $(Hf_{0.25}Zr_{0.25}Ce_{0.25})(Y_{0.125}Yb_{0.125})O_{2-\delta}$, HEFO4B: $(Hf_{0.2}Zr_{0.2}Ce_{0.2})(Y_{0.2}Yb_{0.2})O_{2-\delta}$, HEFO5A: $(Hf_{0.25}Zr_{0.25}Ce_{0.25})(Y_{0.125}Ca_{0.125})O_{2-\delta}$, HEFO7A: $(Hf_{0.25}Zr_{0.25}Ce_{0.25})(Y_{0.125}Gd_{0.125})O_{2-\delta}$, HEF O7B: $(Hf_{0.2}Zr_{0.2}Ce_{0.2})(Y_{0.2}Gd_{0.2})O_{2-\delta}$, HEFO8A: $(Hf_{0.25}Zr_{0.25}Ce_{0.25})(Yb_{0.125}Gd_{0.125})O_{2-\delta}$ and HEFO8B: $(Hf_{0.2}Zr_{0.2}Ce_{0.2})(Yb_{0.2}Gd_{0.2})O_{2-\delta}$, all of which exhibit single solid-solution phases of the fluorite structure.

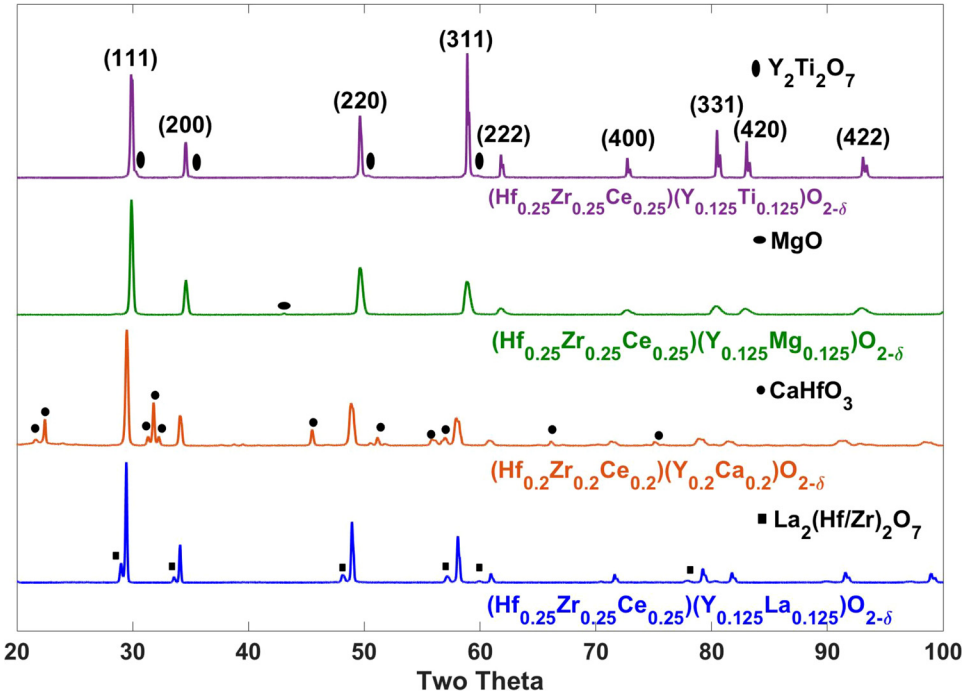

Fig. 2. XRD patterns of HEFO2A: $(Hf_{0.25}Zr_{0.25}Ce_{0.25})(Y_{0.125}Ti_{0.125})O_{2-\delta}$, HEFO3A: $(Hf_{0.25}Zr_{0.25}Ce_{0.25})(Y_{0.125}Mg_{0.125})O_{2-\delta}$, HEF O5B: $(Hf_{0.2}Zr_{0.2}Ce_{0.2})(Y_{0.2}Ca_{0.2})O_{2-\delta}$, HEFO6A: $(Hf_{0.25}Zr_{0.25}Ce_{0.25})(Y_{0.125}La_{0.125})O_{2-\delta}$, all of which possess secondary phases. In all four cases, the primary phases are still solid-solution phases of the fluorite structure.

parameters of the pellets. The relative densities were calculated utilizing theoretical densities computed utilizing an ideal stoichiometry and the lattice parameter measured by XRD.

2.3. Measurements of Thermal/Electrical conductivities and hardness

Thermal conductivities were measured using time-domain thermoreflectance [22,23]. A ~90 nm Al film (measured using picosecond acoustics [24]) is thermally evaporated onto each sample to act as a transducer to convert the optical energy to thermal energy. Using a Ti:Sapphire laser emitting a train of subpicosecond pulses at a central wavelength of 800 nm and a repetition rate of 80 MHz, the output is divided into a pump and probe path. The pump, which is modulated at a frequency of 9.8 MHz, was used to heat the sample, while the probe was utilized to monitor the change in reflectivity at the sample surface. A lock-in amplifier was used to isolate these reflectivity changes at the pump modulation frequency. The pump and probe beams were focused with a 5X objective lens to 35 μm and 15 μm $1/e^2$ diameters, respectively. Utilizing a multilayer, radially symmetric heat diffusion model, we extracted the thermal conductivity and Al/HEFO thermal boundary conductance by adjusting these parameters to obtain the best fit to the ratio of in-phase to out-of-phase voltage obtained by the lock-in

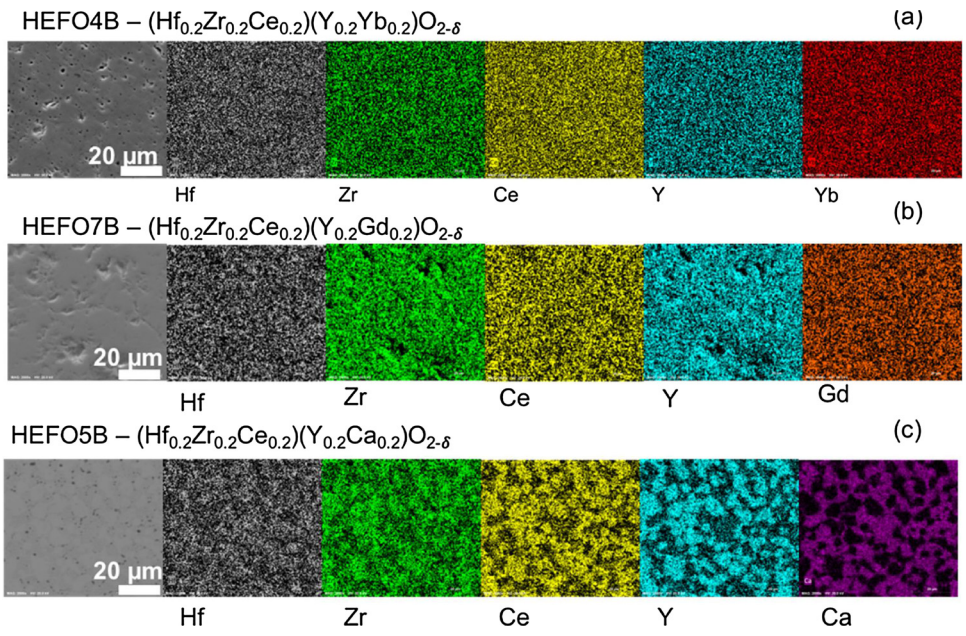

Fig. 3. Cross-sectional SEM images and the corresponding EDS compositional maps of three selected specimens: **(a, b)** HEFO4B: $(Hf_{0.2}Zr_{0.2}Ce_{0.2})(Y_{0.2}Yb_{0.2})O_{2-\delta}$ and HEFO7B: $(Hf_{0.2}Zr_{0.2}Ce_{0.2})(Y_{0.2}Gd_{0.2})O_{2-\delta}$ that exhibit single solid-solution phases with homogeneous compositions and **(c)** HEFO5B: $(Hf_{0.2}Zr_{0.2}Ce_{0.2})(Y_{0.2}Ca_{0.2})O_{2-\delta}$ with a $CaHfO_3$ secondary phase. SEM images and the corresponding EDS compositional maps, along with XRD patterns, of all 12 specimens are documented in the Data Statement.

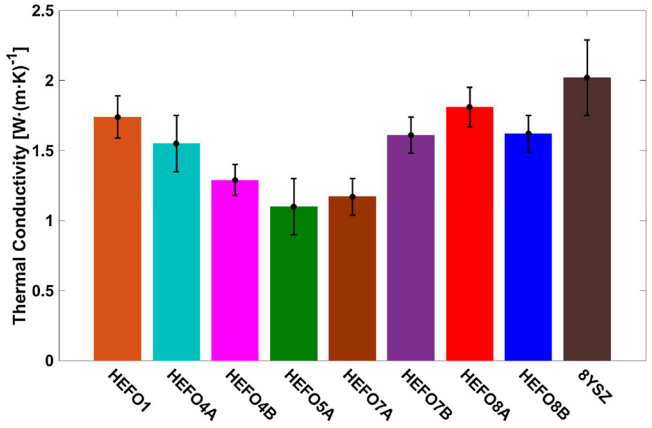

Fig. 4. Thermal conductivities of the eight single-phase HEFOs, along with 8YSZ, measured by TDTR. All HEFOs possess lower thermal conductivities than the fully-dense 8YSZ; three of them, i.e., HEFO4B: $(Hf_{0.2}Zr_{0.2}Ce_{0.2})(Y_{0.2}Yb_{0.2})O_{2-\delta}$, HEFO5A: $(Hf_{0.25}Zr_{0.25}Ce_{0.25})(Y_{0.125}Ca_{0.125})O_{2-\delta}$, and HEFO7A: $(Hf_{0.25}Zr_{0.25}Ce_{0.25})(Y_{0.125}Gd_{0.125})O_{2-\delta}$, show significantly lower thermal conductivities. All specimens were fabricated by the identical process of SPS and subsequent 1500 °C annealing in air.

amplifier [22,25]. The heat capacity of the Al film from a prior report [26] was used. The Al thermal conductivity was obtained from 4-point probe resistivity measurements and applying the Wiedemann–Franz law. Fundamentally, we measured the thermal effusivity of the HEFO to obtain the thermal conductivity. We utilized a rule of mixtures based on the constituent oxides to obtain an estimate of heat capacity for each sample, typically $\sim 3\,J\,cm^{-3}\,K^{-1}$. Uncertainties for the extracted thermal conductivities included those from the repeatability over several spots on the sample, the uncertainty in Al thickness, and the uncertainty in HEFO heat capacity.

Electrical conductivities were measured for compositions HEFO1, HEFO4A, HEFO4B, HEFO5A, and HEFO7B, as well as the 8YSZ reference, with electrochemical impedance spectroscopy (EIS) using an impedance analyzer (Solartron 1255B) in the frequency range of 1 MHz to 1 Hz between 650 and 850 °C at 25 °C intervals with Pt electrodes on both sides of the pellets in zero grade dry air. Platinum pastes were applied to both faces of the samples and subsequently cured at 1000 °C for 10 min prior to conductivity measurements. Total conductivity was determined by fitting Nyquist plots using the Z-View software (Scribner, Inc.). Activation energies for the total conductivities were determined from the Arrhenius plots.

Vicker's hardness measurements were performed on all single-phase high-entropy oxides as well as 8YSZ, pure Y_2O_3, and pure Yb_2O_3 samples (made by the identical HEBM and SPS fabrication procedure) as benchmarks. Hardness measurements were performed with a Vickers' diamond indenter at 200 kgf/mm^2 with a hold time of 15 s. The indentations were examined for conformation with the standard ASTM C1327. The indentations averaged 20–25 μm in width during the testing. Twenty-five measurements were performed at different locations of each specimen; the mean and standard deviation are reported.

3. Results and discussion

3.1. Phase formation and compositional uniformity

After SPS and subsequent 1000 °C annealing in air, a cubic (fluorite-structured), single-phase, solid solution was observed to form in eight different compositions: HEFO1: $(Hf_{0.25}Zr_{0.25}Ce_{0.25}Y_{0.25})O_{2-\delta}$, HEFO4A: $(Hf_{0.25}Zr_{0.25}Ce_{0.25})(Y_{0.125}Yb_{0.125})O_{2-\delta}$, HEFO4B: $(Hf_{0.2}Zr_{0.2}Ce_{0.2})(Y_{0.2}Yb_{0.2})O_{2-\delta}$, HEFO5A: $(Hf_{0.25}Zr_{0.25}Ce_{0.25})(Y_{0.125}Ca_{0.125})O_{2-\delta}$, HEFO7A: $(Hf_{0.25}Zr_{0.25}Ce_{0.25})(Y_{0.125}Gd_{0.125})O_{2-\delta}$, HEFO7B: $(Hf_{0.2}Zr_{0.2}Ce_{0.2})(Y_{0.2}Gd_{0.2})O_{2-\delta}$, HEFO8A: $(Hf_{0.25}Zr_{0.25}Ce_{0.25})(Yb_{0.125}Gd_{0.125})O_{2-\delta}$, and HEFO8B: $(Hf_{0.2}Zr_{0.2}Ce_{0.2})(Yb_{0.2}Gd_{0.2})O_{2-\delta}$ according to the XRD analysis (Fig. 1).

Four other compositions have secondary phases, which were identified using XRD to be $Y_2Ti_2O_7$ in HEFO2A: $(Hf_{0.25}Zr_{0.25}Ce_{0.25})(Y_{0.125}Ti_{0.125})O_{2-\delta}$, MgO in HEFO3A: $(Hf_{0.25}Zr_{0.25}Ce_{0.25})(Y_{0.125}Mg_{0.125})O_{2-\delta}$, $CaHfO_3$ in HEFO5B: $(Hf_{0.2}Zr_{0.2}Ce_{0.2})(Y_{0.2}Ca_{0.2})O_{2-\delta}$, and $La_2(Hf/Zr)_2O_7$ in HEFO6A: $(Hf_{0.25}Zr_{0.25}Ce_{0.25})(Y_{0.125}La_{0.125})O_{2-\delta}$, respectively (Fig. 2). Yet, the major phase is still a cubic fluorite solid-solution phase in each of these four cases.

Furthermore, EDX elemental maps (documented in Supplementary Figures) verified compositional uniformity in the eight specimens of HEFO1, HEFO4A, HEFO4B, HEFO5A, HEFO7A, HEFO7B, HEFO8A, and HEFO8B that XRD suggested the formation of single-phase solid solutions, as well as the presence of the secondary phases in four other compositions (HEFO2A, HEFO3A, HEFO5B, and HEFO6A). Fig. 3 shows three selected (representative) elemental maps of HEFO4B: $(Hf_{0.2}Zr_{0.2}Ce_{0.2})(Y_{0.2}Yb_{0.2})O_{2-\delta}$ and HEFO7B: $(Hf_{0.2}Zr_{0.2}Ce_{0.2})(Y_{0.2}Gd_{0.2})O_{2-\delta}$, where single solid-solution phases formed, and

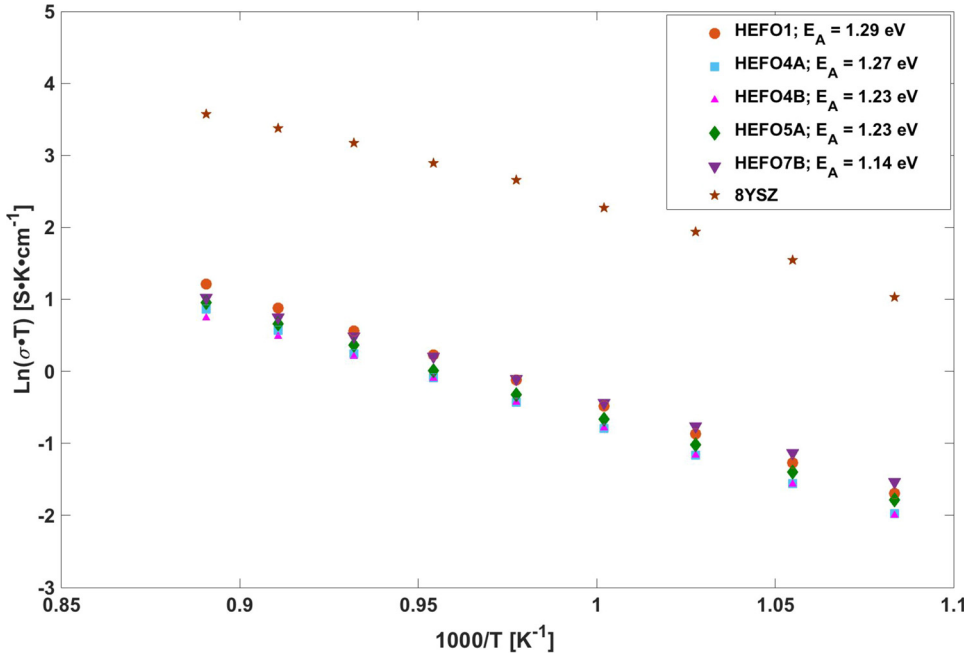

Fig. 5. Arrhenius plots of measured conductivities for five single-phase HEFO, along with 8YSZ, from 650 °C to 850 °C (measured in zero grade dry air).

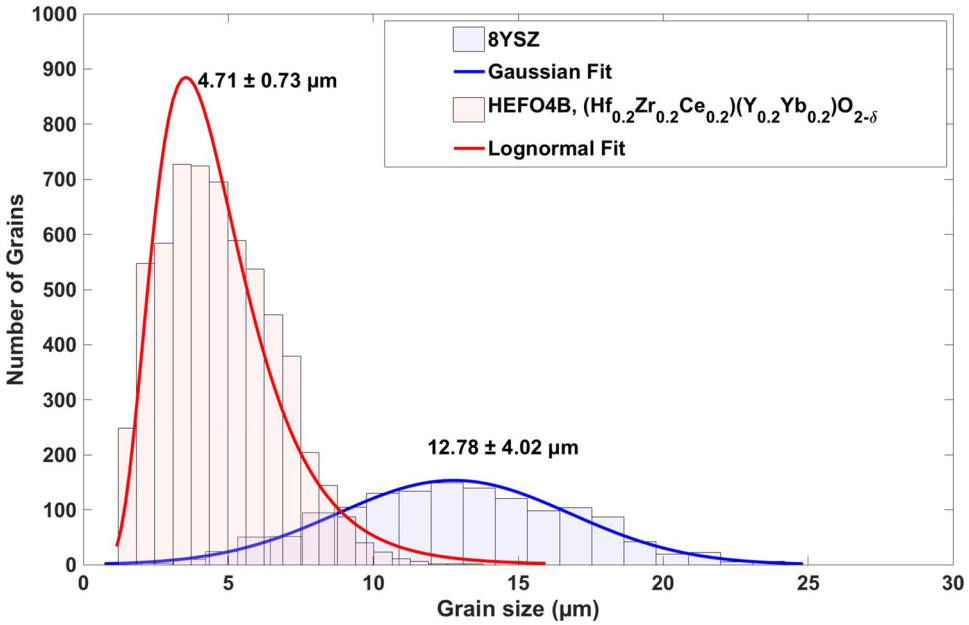

Fig. 6. Grain size distributions of HEFO4B: $(Hf_{0.2}Zr_{0.2}Ce_{0.2})(Y_{0.2}Yb_{0.2})O_{2-\delta}$ and 8YSZ. Both specimens were fabricated by the identical process of SPS and subsequent 1500 °C annealing in air.

HEFO5B: $(Hf_{0.2}Zr_{0.2}Ce_{0.2})(Y_{0.2}Ca_{0.2})O_{2-\delta}$, where a $CaHfO_3$ secondary phase formed.

The eight single-phase solutions all have high configurational entropies contributed from the cation sublattices, i.e., 1.39*R*/mole (i.e., 1.39*R* per mole of $(Hf_{0.25}Zr_{0.25}Ce_{0.25}Y_{0.25})O_{2-\delta}$) for HEFO1, 1.56*R*/mole for HEFO4A, HEFO5A, HEFO7A, and HEFO8A, and 1.61*R*/mole for HEFO4B, HEFO7B, and HEFO8B. In this regard, this term "high entropy" is adopted here because of its historical significance and only implies that these HEFOs have relatively higher configurational entropies per mole of metal cations, in comparison with conventional fluorite oxides such as YSZ.

It is also important to note that here we only count the configurational entropy contribution from the cation (metal ions) sublattice and normalize it to per mole of the oxide chemical formula (that contains one mole of metal cations). There is an additional configurational entropy contribution from the anion sublattice due to the oxygen vacancies, which is much smaller.

3.2. Sintered densities

The relative densities of sintered specimens for all single-phase materials were calculated based on the measured densities and theoretical densities computed from XRD lattice parameters and listed in Table 1. Most sintered samples achieved over ~95% of their respective theoretical densities after the SPS and 1500 °C annealing, with the only two exceptions of HEFO8A: $(Hf_{0.25}Zr_{0.25}Ce_{0.25})(Yb_{0.125}Gd_{0.125})\ O_{2-\delta}$ (77.8% relative density) and HEFO8B: $(Hf_{0.2}Zr_{0.2}Ce_{0.2})(Yb_{0.2}Gd_{0.2})O_{2-\delta}$ (68.4% relative density). The lower densities observed in HEFO8A and

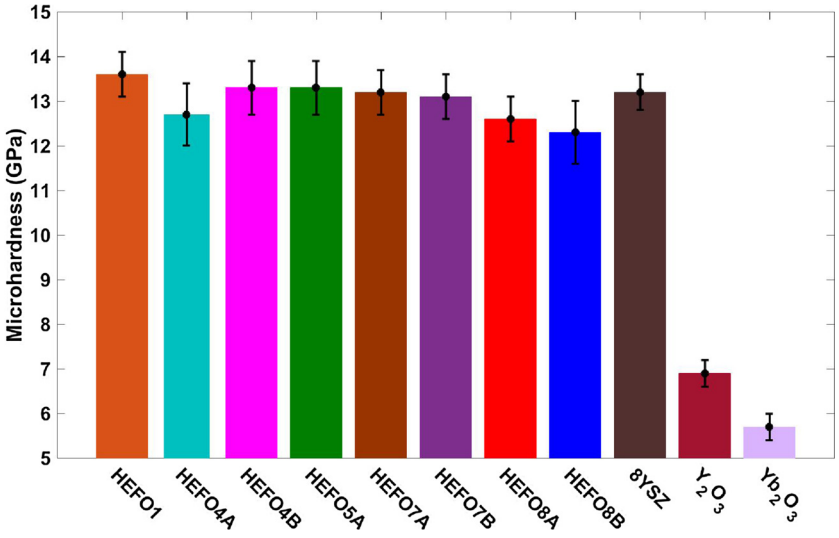

Fig. 7. Measured hardness of eight single-phase HEFO along with 8YSZ, Y_2O_3 and Yb_2O_3 for comparison.

HEFO8B containing both Yb and Gd are likely related to the sluggish diffusion of the heavy/large rare earth cations in the lattice. In fact, ceria and zirconia based ceramics are known to have poor sintering characteristics as the size of dopant cations increases [27–29].

3.3. Thermal conductivity

The thermal conductivities of YSZ have been extensively studied due to its use as a thermal barrier coating at high temperatures. The conductivity is observed to be dependent upon the porosity, fabrication method, and doping level. The thermal conductivity of our 8YSZ specimen, fabricated using the same methods as our HEFOs, was measured to be 2.02 ± 0.17 W/m-K, which is in good agreement with literature for fully-dense, polycrystalline 8YSZ [30].

The measured thermal conductivities of eight single-phase HEFOs are all lower than that of 8YSZ (Fig. 4). Specifically, HEFO5A: $(Hf_{0.25}Zr_{0.25}Ce_{0.25})(Y_{0.125}Ca_{01.25})$ $O_{2-\delta}$ (with 98.5% relative density) possesses the lowest thermal conductivity of 1.1 ± 0.2 W/m-K, followed by HEFO4B and HEFO7A. The reduced thermal conductivities in HEFOs are likely related to increased phonon scattering in the system due to multiple metal cations, which can lead to reductions in the phonon mean free path due to scattering from mass and bond disorder [31,32].

Both grain sizes and porosity can affect thermal conductivity, in addition to the intrinsic effects. On one hand, significant phonon scattering at the grain boundaries is not expected to be a major factor due to the large grain size of 1–3 μm of the HEFOs. On the other hand, the porosity in the two less dense HEFO8A; $(Hf_{0.25}Zr_{0.25}Ce_{0.25})$ $(Yb_{0.125}Gd_{01.25})$ $O_{2-\delta}$ (~78% relative density) and HEFO8B: $(Hf_{0.2}Zr_{0.2}Ce_{0.22})(Yb_{0.2}Gd_{0.2})$ $O_{2-\delta}$ (~68% relative density) can reduce their thermal conductivities. Thus, we expect fully-dense specimens of these two compositions should possess higher thermal conductivities. Note, all six other HEFOs are dense (~94% to 100% relative densities). Overall, we can conclude that high-entropy effects do appear to reduce thermal conductivities in general.

3.4. Electrical conductivity

The measured electrical conductivities of HEFOs and the 8YSZ reference in zero-grade dry air between 650 °C and 850 °C are shown in Fig. 5. HEFOs generally have significantly lower conductivities than 8YSZ. Arrhenius plots [$\ln(\sigma T)$ *vs.* $1000/T$] of the electrical conductivities were used to find the activation energies. Since the platinum electrode is not blocking (for electrons and holes), the measured conductivities include both electronic and (oxygen) ionic contributions. All the HEFOs examined possess similar activation energies of 1.14–1.29 eV and nearly identical conductivity values.

The conductivities of the 8YSZ specimen are approximately an order of magnitude higher than the HEPOs. This is not surprising, as an optimal amount of doping into zirconia and ceria based ceramics exists (e.g., ~ 8 mol. % Y_2O_3 in YSZ) [33,34] and our HEFOs have much higher doping levels (e.g., equivalent to ~14 mol. % in HEFO1 or HEFO4A, and ~25 mol. % in HEFO4B). In addition, partial substitution of CaO (a dopant used in HEFO5A) into the YSZ lattice is observed to depress the overall conductivity at lower temperatures [35].

Another factor that can affect ionic conductivity of fluorite oxides is the grain size [36]. Our HEFOs generally have smaller grain sizes than the 8YSZ reference, which can also contribute to lower overall conductivities. Electron backscattering diffraction (EBSD) was used to determine the grain size distributions in both the 8YSZ reference sample and HEFO4B: $(Hf_{0.2}Zr_{0.2}Ce_{0.2})$ $(Yb_{0.2}Gd_{0.2})O_{2-\delta}$ as examples. The average grain size of HEFO4B is 4.71 ± 0.73 μm, while that of the 8YSZ is 12.78 ± 4.02 μm, as is shown in Fig. 6. The smaller grain sizes in HEFOs may be due to "sluggish kinetics" of grain growth of high-entropy materials, and they can reduce the overall electrical conductivities due to the well-known high grain boundary resistance in fluorite oxides.

3.5. Hardness

The measured Vicker's hardness values of eight single-phase HEFO specimens are in the range of 12.3 to 13.6 GPa, which are comparable with that of an 8YSZ specimen fabricated via the identical procedure (13 ± 0.5 GPa), as shown in Fig. 7 and Table 1. The reported hardness of doped zirconia and ceria based ceramics varies from 6 to 13.5 GPa, with ceria based ceramics leaning towards lower values [19,37–39]. Pure Y_2O_3 and Yb_2O_3 were also fabricated utilizing the identical procedure for testing to benchmark, which possess significantly lower hardness values of 6.9 ± 0.3 GPa and 5.7 ± 0.3 GPa, respectively. XRD characterization verified that the pure Y_2O_3 and Yb_2O_3, as well as 8YSZ, all showed single cubic phases. HEFO8A: $(Hf_{0.25}Zr_{0.25}Ce_{0.25})$ $(Yb_{0.125}Gd_{0.125})O_{2-\delta}$ and HEFO8B: $(Hf_{0.2}Zr_{0.2}Ce_{0.2})$ $(Yb_{0.2}Gd_{0.2})$ $O_{2-\delta}$ are slightly softer in comparison with other HEFOs due to their higher porosities. In summary, the eight HEFOs all possess hardness values (with a mean of 13.25 GPa and a standard deviation of 0.5 GPa) comparable to that of 8YSZ (13 GPa for our specimen fabricated using the same procedure, similar to that reported in Refs [40,41]), despite higher contents of the softer components of Y_2O_3 and Yb_2O_3.

4. Conclusions

Eight single-phase HEFOs or high-entropy fluorite oxides were fabricated via high-energy ball milling, spark plasma sintering, and annealing. The high-entropy fluorite oxides exhibit hardness values comparable to that of the 8YSZ reference (despite high contents of softer components such as Y_2O_3 and Yb_2O_3) and possess lower electrical conductivities. Notably, these HEFOs shows promising potential as low thermal conductivity materials, which are likely a result of the multiple different cation species leading to phonon scattering due tomass and bond disorder.

Acknowledgements

We acknowledge the partial financial support from an Office of Naval Research MURI program (grant no. N00014-15-1-2863) and we thank our Program Mangers Dr. Kenny Lipkowitz and Dr. Eric Wuchina, Principle Investigator Professor Donald Brenner, and all other MURI colleagues for guidance, encouragement, and helpful scientific discussion. H.V. acknowledges NSF for an REU supplement (grant no. CMMI-1436305) on studying the sintering of high-entropy oxides and J.L. also acknowledges partial support of a Vannevar Bush Faculty Fellowship (via ONR Grant No. N00014-16-1-2569). P.E.H. also acknowledges partial support from the National Science Foundation (grant no. CBET-1706388).

Appendix A. Supplementary data

Supplementary material related to this article can be found, in the online version, at doi: https://doi.org/10.1016/j.jeurceramsoc.2018.04.010.

References

[1] D.B. Miracle, O.N. Senkov, A critical review of high entropy alloys and related concepts, Acta Mater. 122 (2017) 448–511, http://dx.doi.org/10.1016/j.actamat.2016.08.081.
[2] J.-W. Yeh, S.-K. Chen, S.-J. Lin, J.-Y. Gan, T.-S. Chin, T.-T. Shun, C.-H. Tsau, S.-Y. Chang, Nanostructured high-entropy alloys with multiple principal elements: novel alloy design concepts and outcomes, Adv. Eng. Mater. 6 (2004) 299–303, http://dx.doi.org/10.1002/adem.200300567.
[3] O.N. Senkov, G.B. Wilks, D.B. Miracle, C.P. Chuang, P.K. Liaw, Refractory high-entropy alloys, Intermetallics 18 (2010) 1758–1765, http://dx.doi.org/10.1016/j.intermet.2010.05.014.
[4] J.-W. Yeh, S.-J. Lin, T.-S. Chin, J.-Y. Gan, S.-K. Chen, T.-T. Shun, C.-H. Tsau, S.-Y. Chou, Formation of simple crystal structures in Cu-Co-Ni-Cr-Al-Fe-Ti-V alloys with multiprincipal metallic elements, Metall. Mater. Trans. A 35 (2004) 2533–2536, http://dx.doi.org/10.1007/s11661-006-0234-4.
[5] B. Cantor, I.T.H. Chang, P. Knight, A.J.B. Vincent, Microstructural development in equiatomic multicomponent alloys, Mater. Sci. Eng. A 375–377 (2004) 213–218, http://dx.doi.org/10.1016/j.msea.2003.10.257.
[6] C.M. Rost, E. Sachet, T. Borman, A. Moballegh, E.C. Dickey, D. Hou, J.L. Jones, S. Curtarolo, J.-P. Maria, Entropy-stabilized oxides, Nat. Commun. 6 (2015) 8485, http://dx.doi.org/10.1038/ncomms9485.
[7] D. Bérardan, S. Franger, D. Dragoe, A.K. Meena, N. Dragoe, Colossal dielectric constant in high entropy oxides, Phys. Status Solidi RRL – Rapid Res. Lett. 10 (2016) 328–333, http://dx.doi.org/10.1002/pssr.201600043.
[8] D. Bérardan, S. Franger, A.K. Meena, N. Dragoe, Room temperature lithium superionic conductivity in high entropy oxides, J. Mater. Chem. A 4 (2016) 9536–9541, http://dx.doi.org/10.1039/C6TA03249D.
[9] V. Braic, A. Vladescu, M. Balaceanu, C.R. Luculescu, M. Braic, Nanostructured multi-element (TiZrNbHfTa)N and (TiZrNbHfTa)C hard coatings, Surf. Coat. Technol. 211 (2012) 117–121, http://dx.doi.org/10.1016/j.surfcoat.2011.09.033.
[10] M.-H. Hsieh, M.-H. Tsai, W.-J. Shen, J.-W. Yeh, Structure and properties of two Al–Cr–Nb–Si–Ti high-entropy nitride coatings, Surf. Coat. Technol. 221 (2013) 118–123, http://dx.doi.org/10.1016/j.surfcoat.2013.01.036.
[11] J. Gild, Y. Zhang, T. Harrington, S. Jiang, T. Hu, M.C. Quinn, W.M. Mellor, N. Zhou, K. Vecchio, J. Luo, High-Entropy metal diborides: a new class of high-entropy materials and a new type of ultrahigh temperature ceramics, Sci. Rep. 6 (2016) 37946, http://dx.doi.org/10.1038/srep37946.
[12] S. Jiang, T. Hu, J. Gild, N. Zhou, J. Nie, M. Qin, T. Harrington, K. Vecchio, J. Luo, A new class of high-entropy perovskite oxides, Scr. Mater. 142 (2018) 116–120, http://dx.doi.org/10.1016/j.scriptamat.2017.08.040.
[13] R. Djenadic, A. Sarkar, O. Clemens, C. Loho, M. Botros, V.S.K. Chakravadhanula, C. Kübel, S.S. Bhattacharya, A.S. Gandhi, H. Hahn, Multicomponent equiatomic rare earth oxides, Mater. Res. Lett. 5 (2017) 102–109, http://dx.doi.org/10.1080/21663831.2016.1220433.
[14] A.G. de la Obra, M.A. Avilés, Y. Torres, E. Chicardi, F.J. Gotor, A new family of cermets: chemically complex but microstructurally simple, Int. J. Refract. Met. Hard Mater. 63 (2017) 17–25, http://dx.doi.org/10.1016/j.ijrmhm.2016.04.011.
[15] R. Liu, H. Chen, K. Zhao, Y. Qin, B. Jiang, T. Zhang, G. Sha, X. Shi, C. Uher, W. Zhang, L. Chen, Entropy as a gene-like performance indicator promoting thermoelectric materials, Adv. Mater. 29 (2017), http://dx.doi.org/10.1002/adma.201702712 n/a–n/a.
[16] X.Q. Cao, R. Vassen, D. Stoever, Ceramic materials for thermal barrier coatings, J. Eur. Ceram. Soc. 24 (2004) 1–10, http://dx.doi.org/10.1016/S0955-2219(03)00129-8.
[17] S.J. Skinner, J.A. Kilner, Oxygen ion conductors, Mater. Today 6 (2003) 30–37, http://dx.doi.org/10.1016/S1369-7021(03)00332-8.
[18] M.N. Tsampas, F.M. Sapountzi, P. Vernoux, Applications of yttria stabilized zirconia (YSZ) in catalysis, Catal. Sci. Technol. 5 (2015) 4884–4900, http://dx.doi.org/10.1039/C5CY00739A.
[19] Y.-P. Fu, S.-H. Chen, J.-J. Huang, Preparation and characterization of Ce0.8M0.2O2 − δ (M = Y, Gd, Sm, Nd, La) solid electrolyte materials for solid oxide fuel cells, Int. J. Hydrog. Energy 35 (2010) 745–752, http://dx.doi.org/10.1016/j.ijhydene.2009.10.093.
[20] N.M. Sammes, Z. Cai, Ionic conductivity of ceria/yttria stabilized zirconia electrolyte materials, Solid State Ionics 100 (1997) 39–44, http://dx.doi.org/10.1016/S0167-2738(97)00306-8.
[21] J. Cho, J. Park, J. An, Low thermal conductivity of atomic layer deposition yttria-stabilized zirconia (YSZ) thin films for thermal insulation applications, J. Eur. Ceram. Soc. 37 (2017) 3131–3136, http://dx.doi.org/10.1016/j.jeurceramsoc.2017.03.045.
[22] D.G. Cahill, Analysis of heat flow in layered structures for time-domain thermoreflectance, Rev. Sci. Instrum. 75 (2004) 5119–5122, http://dx.doi.org/10.1063/1.1819431.
[23] A.J. Schmidt, Pump-probe thermoreflectance, Annu. Rev. Heat Transf. 16 (2013) 159–181, http://dx.doi.org/10.1615/AnnualRevHeatTransfer.v16.60.
[24] C. Thomsen, H.J. Maris, J. Tauc, Picosecond acoustics as a non-destructive tool for the characterization of very thin films, Thin Solid films 154 (1987) 217–223, http://dx.doi.org/10.1016/0040-6090(87)90366-X.
[25] J.L. Braun, P.E. Hopkins, Upper limit to the thermal penetration depth during modulated heating of multilayer thin films with pulsed and continuous wave lasers: a numerical study, J. Appl. Phys. 121 (2017) 175107, http://dx.doi.org/10.1063/1.4982915.
[26] Y.S. Touloukian, E.H. Buyco, Specific Heat: Metallic Elements and Alloys, IFI/Plenum, New York, 1970.
[27] E. Suda, B. Pacaud, M. Mori, Sintering characteristics, electrical conductivity and thermal properties of La-doped ceria powders, J. Alloys Compd. 408 (2006) 1161–1164, http://dx.doi.org/10.1016/j.jallcom.2004.12.135.
[28] V.V. Kharton, F.M.B. Marques, A. Atkinson, Transport properties of solid oxide electrolyte ceramics: a brief review, Solid State Ion. 174 (2004) 135–149, http://dx.doi.org/10.1016/j.ssi.2004.06.015.
[29] D.P.F.D. Souza, A.L. Chinelatto, M.F.D. Souza, Impure zirconia electrical conductivity enhancement by rare-earth minority ions in the Y2O3 RE2O3 ZrO2 system, J. Mater. Sci. 30 (1995) 4355–4362, http://dx.doi.org/10.1007/BF00361517.
[30] K.W. Schlichting, N.P. Padture, P.G. Klemens, Thermal conductivity of dense and porous yttria-stabilized zirconia, J. Mater. Sci. 36 (2001) 3003–3010, http://dx.doi.org/10.1023/A:1017970924312.
[31] A. Giri, J.L. Braun, C.M. Rost, P.E. Hopkins, On the minimum limit to thermal conductivity of multi-atom component crystalline solid solutions based on impurity mass scattering, Scr. Mater. 138 (2017) 134–138, http://dx.doi.org/10.1016/j.scriptamat.2017.05.045.
[32] A. Giri, J.L. Braun, P.E. Hopkins, Reduced dependence of thermal conductivity on temperature and pressure of multi-atom component crystalline solid solutions, J. Appl. Phy. 123 (2018) article number: 015106.
[33] S.M. Haile, Fuel cell materials and components, Acta Mater. 51 (2003) 5981–6000, http://dx.doi.org/10.1016/j.actamat.2003.08.004.
[34] J.A. Kilner, Fast oxygen transport in acceptor doped oxides, Solid State Ionics 129 (2000) 13–23, http://dx.doi.org/10.1016/S0167-2738(99)00313-6.
[35] J. Gong, Y. Li, Z. Tang, Z. Zhang, Ionic conductivity in the ternary system (ZrO2)1 − 0.08x − 0.12y–(Y2O3)0.08x–(CaO)0.12y, J. Mater. Sci. 35 (2000) 3547–3551, http://dx.doi.org/10.1023/A:1004857312129.
[36] X.J. Chen, K.A. Khor, S.H. Chan, L.G. Yu, Influence of microstructure on the ionic conductivity of yttria-stabilized zirconia electrolyte, Mater. Sci. Eng. A 335 (2002) 246–252, http://dx.doi.org/10.1016/S0921-5093(01)01935-9.
[37] I. Abraham, G. Gritzner, Mechanical properties of doped cubic zirconia ceramics, J. Mater. Sci. Lett. 12 (1993) 995–997, http://dx.doi.org/10.1007/BF00420197.
[38] S. Sameshima, T. Ichikawa, M. Kawaminami, Y. Hirata, Thermal and mechanical properties of rare earth-doped ceria ceramics, Mater. Chem. Phys. 61 (1999) 31–35, http://dx.doi.org/10.1016/S0254-0584(99)00109-1.
[39] T. Sakuma, Y.-I. Yoshizawa, H. Suto, The microstructure and mechanical properties of yttria-stabilized zirconia prepared by arc-melting, J. Mater. Sci. 20 (1985) 2399–2407, http://dx.doi.org/10.1007/BF00556069 (n.d.).
[40] P. Dahl, I. Kaus, Z. Zhao, M. Johnsson, M. Nygren, K. Wiik, T. Grande, M.-A. Einarsrud, Densification and properties of zirconia prepared by three different sintering techniques, Ceram. Int. 33 (2007) 1603–1610, http://dx.doi.org/10.1016/j.ceramint.2006.07.005.
[41] M. Mazaheri, M. Valefi, Z.R. Hesabi, S.K. Sadrnezhaad, Two-step sintering of nanocrystalline 8Y2O3 stabilized ZrO2 synthesized by glycine nitrate process, Ceram. Int. 35 (2009) 13–20, http://dx.doi.org/10.1016/j.ceramint.2007.09.009.